Sensitivity studies for the weak r process: neutron capture rates

R. Surman, M. Mumpower, R. Sinclair, K. L. Jones, W. R. Hix, and G. C. McLaughlin

---

Articles you may be interested in

Challenges in nucleosynthesis of trans-iron elements
AIP Advances **4**, 041012 (2014); 10.1063/1.4868239

Sensitivity studies for the main r process: β-decay rates
AIP Advances **4**, 041009 (2014); 10.1063/1.4867192

Neutron captures and the rprocess
AIP Conf. Proc. **819**, 419 (2006); 10.1063/1.2187894

The weak sprocess and its relation to explosive nucleosynthesis
AIP Conf. Proc. **819**, 265 (2006); 10.1063/1.2187869

Cross section measurements of capture reactions relevant to the p process: Status and perspectives
AIP Conf. Proc. **704**, 422 (2004); 10.1063/1.1737137

Sensitivity studies for the weak *r* process: neutron capture rates

R. Surman,[1,a] M. Mumpower,[2] R. Sinclair,[3] K. L. Jones,[3] W. R. Hix,[3,4] and G. C. McLaughlin[5]

[1]*Department of Physics and Astronomy, Union College, Schenectady, NY 12308 USA*
[2]*Department of Physics, University of Notre Dame, Notre Dame, IN 46556 USA*
[3]*Department of Physics and Astronomy, University of Tennessee, Knoxville, TN 37996 USA*
[4]*Physics Division, Oak Ridge National Laboratory, Oak Ridge, TN 37831 USA*
[5]*Department of Physics, North Carolina State University, Raleigh, NC 27695 USA*

Rapid neutron capture nucleosynthesis involves thousands of nuclear species far from stability, whose nuclear properties need to be understood in order to accurately predict nucleosynthetic outcomes. Recently sensitivity studies have provided a deeper understanding of how the *r* process proceeds and have identified pieces of nuclear data of interest for further experimental or theoretical study. A key result of these studies has been to point out the importance of individual neutron capture rates in setting the final *r*-process abundance pattern for a 'main' ($A \sim 130$ peak and above) *r* process. Here we examine neutron capture in the context of a 'weak' *r* process that forms primarily the $A \sim 80$ *r*-process abundance peak. We identify the astrophysical conditions required to produce this peak region through weak *r*-processing and point out the neutron capture rates that most strongly influence the final abundance pattern. © *2014 Author(s). All article content, except where otherwise noted, is licensed under a Creative Commons Attribution 3.0 Unported License.* [http://dx.doi.org/10.1063/1.4867191]

I. INTRODUCTION

In the 1950s it was recognized that the solar system abundances of nuclei heavier than iron could be divided roughly in half based on the nucleosynthesis processes that create them.[1,2] Slow neutron capture process, or *s*-process, nuclei lie along the middle of the valley of stability, and rapid neutron capture process, or *r*-process, nuclei are found on the neutron-rich side of stability. A third process, the *p* process, is responsible for the significantly less abundant nuclei on the proton-rich side of stability. Since that time much progress has been made, e.g. Ref. 3, and the basic mechanisms of and astrophysical sites for the creation of the *s*-process[4] and heavy *p*-process[5,6] nuclei are on a firm footing. The largest remaining open questions involve the site of the synthesis of the heaviest elements ($A > 130$) in the *r* process, and the uncertain origins of the elements above the iron peak ($80 < A < 130$).

The solar *r*-process abundance pattern traditionally consists of three main abundance peaks around $A \sim 80$, 130, and 195, associated with the $N = 50$, 82, and 126 closed neutron shells. The locations of the peaks in *A* show that they must have formed in neutron-rich conditions, with the higher-mass peaks requiring greater neutron-richness than the lighter-mass peak. Thus the astrophysical conditions required to produce a good match to the $A \sim 80$ solar abundance pattern are distinct from those required to make the heavier peaks.[7] Observational data also points to separate origins for these nuclei, with the first hint coming from meteoritic data.[8] More recently, spectroscopic studies of low metallicity halo stars have been performed that show for the most part a solar *r*-process

---

[a]Electronic mail: surmanr@union.edu

4, 041008-1

pattern for elements from barium to lead ('main' *r* process) but large scatter below barium.[9] It may be that these light elements owe their origins to a range of nucleosynthesis processes, some of which may even be proton-rich; the question is difficult to answer without isotopic information for the halo star abundances (see, e.g., Ref. 10 and references therein). Given this uncertainty, the production mechanism for these elements has often been dubbed the light element primary process, or LEPP.

Studies of $A \sim 80$ nucleosynthesis are additionally complicated by large uncertainties in nuclear physics data of the short-lived, exotic nuclei that assumably participate in the processes. These nuclei are difficult to measure in the laboratory owing to the small production cross sections and short lifetimes. Nuclei that participate in the *r*-process typically have half lives that are too short to allow them to be made into a target (i.e. less than at least a month). As neutron targets are not available, neutron capture experiments cannot be performed on these nuclei. Nuclear data relevant to *r*-process calculations (J^π assignments, excitation energies, spectroscopic factors) can however be extracted from transfer reactions, such as (d, p). To date, only a few short-lived, neutron-rich nuclei in the mass 80 to 140 region have been investigated via (d, p) reactions.[11–17] These measurements were all performed at the Holifield radioactive ion beam facility,[18] which has since ceased operations as a user facility. It is expected that research in this area will resume once the appropriate capabilities are developed at current and next generation facilities. Even then, many interesting nuclear species will still lie outside the reach of anticipated experimental investigations and so their properties need to be calculated using nuclear models.

For a main *r* process, the pieces of nuclear data that most strongly impact the predicted abundances have been identified via sensitivity studies.[19–23] A sensitivity study begins with the choice of a baseline astrophysical simulation. Then an individual nuclear parameter, such as mass, β-decay rate or neutron capture rate, is varied, the simulation is repeated, and the final abundance patterns are compared. This process is repeated for each parameter of interest in the network. While sensitivity studies for masses, β-decay rates, and neutron capture rates have been performed for a main *r* process, $80 < A < 100$ nucleosynthesis has only been addressed on the proton-rich side[24] and for a weak *s* process.[25] The importance of neutron capture rates for a main *r* process has also been discussed in Refs. 26–30.

Here we extend the neutron capture rate sensitivity studies of Ref. 20 and 21 to nuclei below the $A \sim 130$ *r*-process peak. While we recognize that these nuclei may have multiple nucleosynthetic origins, here we will address only a potential weak *r* process—a rapid neutron capture process that forms a solar-type $A \sim 80$ *r*-process peak and potentially nuclei up to the $A \sim 130$ peak. Though neutron capture rates may play a role in a proton-rich LEPP, we will not discuss it here. In Section II, we identify astrophysical conditions appropriate for a weak *r* process. In Section III, we describe our sensitivity studies and review the mechanisms by which individual neutron capture rates in the region of a major *r*-process peak can influence the final abundance pattern. The compiled results identifying the neutron capture rates with the greatest impact on the final isotopic abundances from a weak *r* process are presented in Section IV.

II. ASTROPHYSICAL CONDITIONS

We study a weak *r* process in the context of neutron-rich supernova and collapsar accretion disk winds.[31,32] Wind trajectories are characterized by a measure of heating or entropy per baryon, s/k, the dynamic timescale, τ, that describes the drop in temperature and density, e.g., $\rho \sim e^{-t/\tau}$, and the neutron-richness of the ejected material or electron fraction, Y_e. In order to perform a weak *r*-process sensitivity study, we first need to identify astrophysical conditions that produce these nuclei. We ran many simulations, varying the wind parameters in discrete units of 1 for s/k, 5 ms for τ, and 0.05 for Y_e, as in Ref. 33. To assess how well an abundance pattern matches the solar $A = 80$ data we calculate the deviation,

$$D = \frac{\sum_{A=75}^{A=85}(\alpha Y(A) - Y_{solar}(A))^2}{\sum_{A=75}^{A=85} Y_{solar}^2(A)} \tag{1}$$
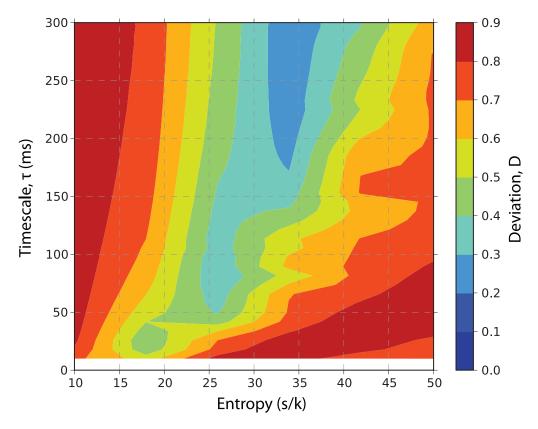
FIG. 1. Shows the calculated deviation, D, from solar for a slice of astrophysical parameter space with $Y_e = 0.4$. Small deviations (blue) denote conditions which best reproduce the $A = 80$ solar region. The timescale is given in units of milliseconds.

where abundances, $Y(A) = X(A)/A$, are computed from the atomic mass, A, and the mass fraction along an isobaric chain, $X(A) = \sum_{A=Z+N} X(Z, N)$ (note mass fractions for any simulation will sum to 1, $\sum_A X(A) = 1$). Each abundance curve is scaled to solar by a factor α which is computed by solving:

$$\frac{dD}{d\alpha} = 0 \tag{2}$$

A slice of this astrophysical parameter space at constant $Y_e = 0.4$ is shown in Fig. 1. The best matches to the solar pattern (small deviations) occur between $s/k = 30$ and $s/k = 40$ with timescales longer than $\tau = 0.15$ s. Small deviations also occur outside the range of the parameter space shown in Fig. 1 at constant $Y_e = 0.4$, however we rule these conditions out because they overproduce abundances of the heavier elements.

A sample best fit abundance pattern from the $Y_e = 0.4$ grid of astrophysical parameter space is shown in Fig. 2 (case 3 from Table I, short dashed green line) compared to the solar pattern. Note the $A \sim 80$ peak is reproduced but element synthesis does not proceed beyond it. Heavier nuclei can be made at a slightly lower Y_e, but this has the additional effect of shifting the peak location to higher A, weakening the match to the solar pattern. An example of this effect is shown in Fig. 2 (case 2 from Table I, long dashed blue line). It is a general feature that becomes even more pronounced at higher entropies, which can lead to the so-called $A \sim 90$ overproduction problem in slightly neutron-rich supernova winds.[10,34] The best match to the solar pattern from $70 < A < 110$ seems to be found at lower entropies and lower Y_e's; Fig. 2 shows an example of this as well (case 1 from Table I, solid red line).

In addition to general parameterized trajectories, we also consider trajectories from the supernova neutrino-driven wind simulations used in Ref. 10 and from the black hole-neutron star merger
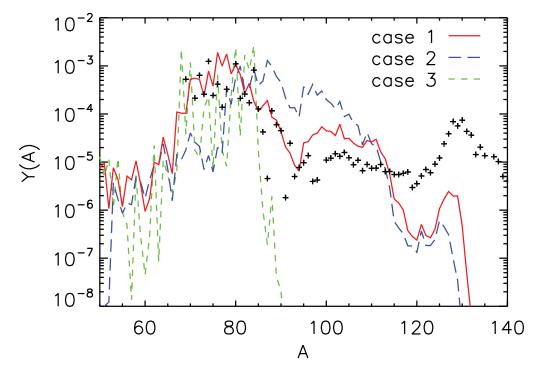
FIG. 2. Shows abundance patterns for three sample weak *r*-process trajectories, with wind conditions listed in Table I for case 1 (red solid line), case 2 (long dashed blue line), and case 3 (short dashed green line). The scaled solar *r*-process residuals (crosses) from Ref. 35 are included for comparison.

TABLE I. Wind conditions for three example weak *r*-process trajectories.

case	s/k	$\tau(s)$	Y_e
1	10	0.20	0.30
2	30	0.10	0.35
3	35	0.30	0.40

accretion disk outflows of Ref. 36. A total of approximately ninety distinct astrophysical trajectories are chosen as baseline simulations for our neutron capture rate sensitivity studies. Included in this set are trajectories that result in an excellent match to the solar weak *r*-process pattern as well as those that make mostly $A \sim 90 - 100$ nuclei; main *r*-process trajectories are excluded.

III. SENSITIVITY STUDY

The sensitivity studies took the baseline weak *r*-process simulations described above as starting points. For each astrophysical trajectory chosen, we determined the baseline abundance pattern with a nuclear network calculation. The nuclear network code employed includes all relevant two- and three-body charged particle reactions, weak reactions, neutron captures, and photodissociations, with reaction rates from JINA REACLIB v1.0.[37] Note all of the REACLIB neutron capture rates relevant here are theoretical values, from NON-SMOKER.[38] We followed the composition from free nucleons and alpha particles in nuclear statistical equilibrium (NSE) through the assembly of seed nuclei by charged particle reactions and the subsequent weak *r* process. The reaction network is described in detail in Ref. 39.

Once the baseline abundance pattern was determined, the neutron capture rates of approximately 300 nuclei in the $A \sim 80$ region and above were individually varied by a constant factor. Theoretical compilations of neutron capture rates can differ from each other by orders of magnitude,[19,20,27] so
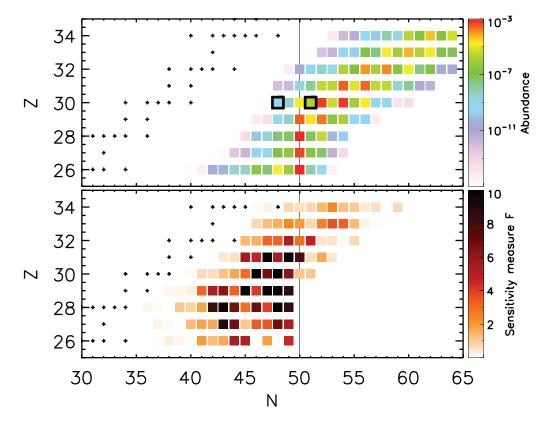
FIG. 3. Sensitivity measures F (bottom panel) resulting from a sensitivity study in which each neutron capture rate in the $A \sim 80$ region is varied by a factor of 100. The baseline simulation is case 1 from Table I and Fig. 2. The top panel shows the abundances at the point in the simulation where the neutron-to-seed ratio is one (at the onset of freezeout). The two boxed nuclei, ^{78}Zn and ^{81}Zn, are singled out for further analysis.

the factor was taken to be 100. With each individual variation, we reran the simulation, and compared the resulting abundance pattern to the baseline pattern using the sensitivity measure F as in Ref. 20:

$$F = 100 \times \sum_A |X(A) - X_{\text{baseline}}(A)| \tag{3}$$

where $X_{\text{baseline}}(A)$ are the final mass fractions of the baseline abundance pattern and $X(A)$ are the final mass fractions for the simulation with the rate change. The outcome of each sensitivity study is thus a set of sensitivity measures F for each of the 300 nuclei whose capture rates were varied.

The resulting sensitivity measures from a single sensitivity study are shown in the bottom panel of Fig. 3 for an astrophysical trajectory with entropy $s/k = 10$, timescale $\tau = 0.2$ s, and electron fraction $Y_e = 0.3$ (case 1 from Table I). These conditions are similar to those that may be obtained in the winds from the accretion disk formed in a compact object merger.[36,40] The final abundance pattern for this baseline simulation is a good match to the solar $A \sim 80$ region and above and as shown in Fig. 2, plotted with the red line. This case is a 'true' weak r process, in that we see the establishment of (n, γ)-(γ, n) equilibrium, and the behavior of the nuclear flow near and through the $N = 50$ closed shell is similar to that in the $N = 82$ and $N = 126$ regions in a main r process, with the r-process path as shown in the top panel of Fig. 3. Thus, we expect the role of neutron capture rates to be similar to that identified for the $N = 82$ region in a main r process, as described in detail in Refs. 19 and 20. Indeed, the pattern of sensitivity measures for this example follow the $N = 82$ region results, with the greatest sensitivity measures F found for nuclei above and to the left of the closed shell, along the β-decay pathways of the closed shell nuclei, as seen in Fig. 3.

Refs. 19 and 20 identified two mechanisms by which neutron capture rates in the $A \sim 130$ region influence the final r-process abundance pattern: an early-freezeout photodissociation effect and a

late-freezeout neutron capture effect. Both operate toward the end of the *r*-process, after the neutron-to-seed ratio drops below one and (n, γ)-(γ, n) equilibrium begins to fail. If the conditions are still hot at this point, the *r*-process path can begin to move toward stability by photodissociations in addition to β decays. Individual photodissociation rates can therefore become important, particularly for long-lived, highly populated even-*N* nuclei. An increase of the photodissociation rate of a highly populated nucleus, for example, can enhance the shift of material to lower *A*, providing a burst of neutrons that can then be captured by nuclei throughout the network. The late-freezeout neutron capture effect operates later, when the path moves toward stability primarily via β decays and there is competition for the capture of the final few free neutrons. The most important capture rates at this time are for the nuclei along the β-decay pathways of the closed shell nuclei, since these nuclei are so abundant that an increase to the neutron capture rate, for example, can effectively steal neutrons away from the rest of the pattern.

These same two effects operate in this weak *r*-process trajectory, as we show here for two example nuclei in the $A \sim 80$ region in Figs. 3 and 4. The nuclear flow from the equilibrium path nucleus ^{82}Zn to ^{80}Zn as the path begins moving toward stability at the onset of freezeout is controlled by the photodissociation rate of ^{82}Zn, which depends on the capture rate of ^{81}Zn by detailed balance:

$$\lambda_\gamma(Z, A + 1) \propto T^{3/2} \exp\left(\frac{-S_n(Z, A + 1)}{kT}\right) \langle \sigma v \rangle_{(Z,A)} \tag{4}$$

where T is the temperature, S_n is the one-neutron separation energy, and $\langle \sigma v \rangle$ is the thermally-averaged neutron capture rate of the adjacent isotope. An increase in the capture rate of ^{81}Zn by a factor of 100 thus also increases the photodissociation rate of ^{82}Zn by the same factor. Here this shifts material from ^{82}Zn to ^{80}Zn (via ^{81}Zn, which immediately photodissociates to ^{80}Zn) at the beginning of freezeout and results in an associated release of neutrons back into the environment. This is illustrated in the top panel of Fig. 4, which shows the change in the rate at which neutrons are captured in the $70 < A < 90$ region in the simulation with the rate change compared to the baseline simulation. It is negative since the photodissociations result in a net release of neutrons. These neutrons are captured throughout the rest of the network, as also shown in Fig. 4, which subsequently produces changes throughout the abundance pattern. The second example is of a late-freezeout neutron capture effect, for another isotope of zinc, ^{78}Zn. This nucleus is populated in late freezeout from the β-decay chain ^{78}Ni $\rightarrow$ ^{78}Cu $\rightarrow$ ^{78}Zn. When its capture rate is increased, ^{78}Zn captures more of the few remaining free neutrons than in the baseline simulation, which leaves fewer neutrons for capture elsewhere in the network. This is shown in the bottom panel of Fig. 4.

The element synthesis in many of the trajectories studied does not proceed by a clean weak *r* process, however. At moderately higher entropies and initial electron fractions, the nucleosynthetic flow through the $N = 50$ closed shell primarily proceeds via (n, p) and (n, α) reactions.[10,34] Thus the flow has moved beyond the $N = 50$ closed shell by the time charged particle reactions terminate and neutron capture takes over. This is the case for the simulation with $s/k = 30$, $\tau = 0.1$ s, and $Y_e = 0.35$ (case 2 from Table I), with final abundances plotted with the long dashed blue line in Fig. 2 and abundances at a temperature of $T = 1.75$ GK shown in the top panel of Fig. 5. There is sufficient *r*-processing of the material in this example for the early freezeout photodissociation effect and the late freezeout neutron capture effect to operate. However, since the flow has largely moved past $N = 50$, the nuclei with the highest sensitivity measures F are also found at higher Z, N. As shown in the bottom panel of Fig. 5, the highest sensitivity measures are found primarily for nuclei which lie along the β-decay pathways of the most abundant nuclei along the *r*-process path with $30 < Z < 34$.

The final set of trajectories considered have even higher entropies and electron fractions and produce primarily $A \sim 90 - 100$ nuclei. In these cases there is essentially no *r*-processing of the material, as all of the neutrons have been expended in (n, p) and (n, α) reactions by the time the temperature drops to $T \sim 2 - 3$ GK. The simulation with $s/k = 35$, $\tau = 0.3$ s, and $Y_e = 0.4$ (case 3 from Table I), with abundances given by the short dashed green line in Fig. 2, is an example of this. The neutron abundance for this simulation is shown as a function of decreasing temperature in Fig. 6, as compared to the two example simulations described above that do show weak *r*-processing.
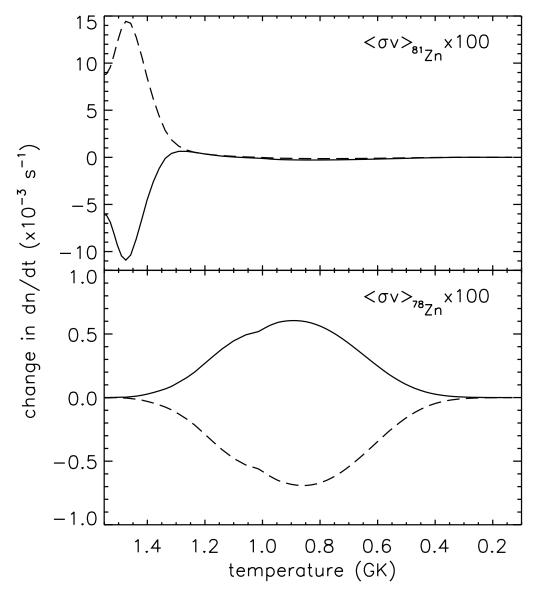
FIG. 4. The resulting change in the rate at which neutrons are captured in the $A \sim 80$ region (solid line) and elsewhere (dashed line) when the neutron capture rate of ^{81}Zn (top panel) or ^{78}Zn (bottom panel) is increased by a factor of 100, compared to a baseline simulation with no neutron capture rate modifications.

Without any neutrons available for late time neutron captures, we see essentially no neutron capture rate sensitivity measures F greater than one for these trajectories.

IV. COMBINED RESULTS

The neutron capture rate sensitivity study procedure was repeated for the approximately ninety astrophysical trajectories chosen for this investigation. Of these, 55 show some significant sensitivity to neutron capture rates. The lower entropy $10 < s/k < 30$, lower electron fraction $Y_e < 0.35$ trajectories that produce a clean weak r-process show neutron capture rate sensitivity measures similar to Fig. 3. Moderate to higher entropy $30 < s/k < 100$ and electron fraction $0.35 < Y_e < 0.48$ trajectories that show partial r-processing show neutron capture rate sensitivity measures similar to Fig. 5. The results from all 55 sensitivity studies, Fig. 7 and Table II, show the maxiumum sensitivity measures F obtained in the full set of studies.
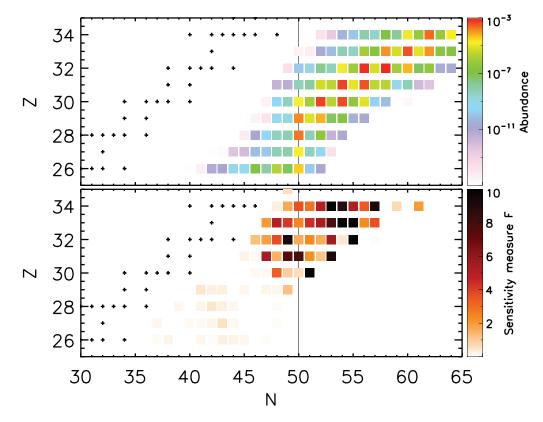
FIG. 5. Similar to Fig. 3, but for baseline simulation case 2 from Table I and Fig. 2.
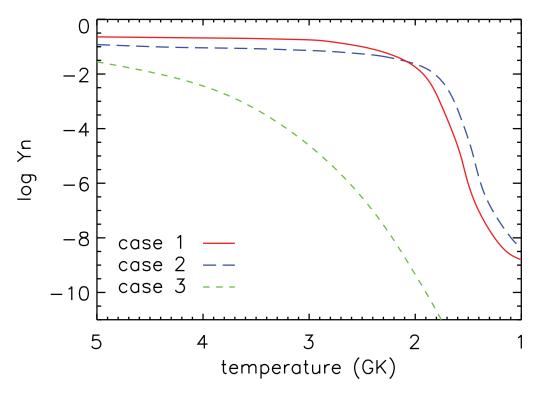

FIG. 6. Neutron abundance as a function of decreasing temperature for the three baseline simulations from Table I and Fig. 2.
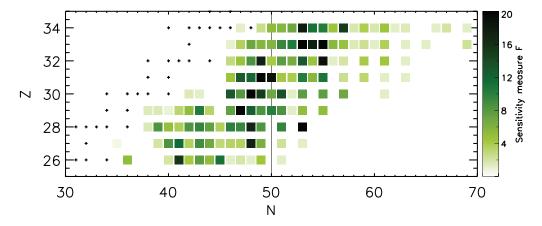
FIG. 7. Combined results of fifty-five neutron capture rate sensitivity studies run under a range of distinct astrophysical conditions. The shading indicates the maximum sensitivity measure F obtained in the full set of sensitivity studies, with the darkest squares indicating maximum F measures of greater than 20. Note nuclei are shaded only if their sensitivity measures F exceed 0.5 in more than one set of astrophysical conditions.

TABLE II. Nuclei with maximum neutron capture rate sensitivity measures $F > 10$ from the combined results of fifty-five neutron capture rate sensitivity studies run under a range of distinct astrophysical conditions, from Fig. 7.

Z	A	F
26	67	15.8
26	71	11.2
27	68	11.6
27	75	17.3
28	76	17.2
28	81	34.1
29	72	10.4
29	74	15.1
29	76	25.0
29	77	12.5
29	79	10.2
30	76	13.1
30	78	23.5
30	79	15.2
30	81	13.6
31	78	12.8
31	79	12.1
31	80	26.0
31	81	18.8
31	84	10.3
31	86	11.0
32	81	17.5
32	85	13.1
32	87	19.1
33	85	10.5
33	86	22.5
33	87	17.8
33	88	22.6
34	87	18.0
34	88	11.2
34	89	10.3
34	91	15.3

V. CONCLUSION

We have examined the role of neutron capture of $A = 80$ nuclei in the context of a weak r process from winds that could occur in supernova or collapsar accretion disks. In the interest of studying neutron capture in these environments we have identified astrophysical conditions which match features of the $A = 80$ solar abundances. The best matches to solar are low entropy $10 < s/k < 30$, low electron fraction $Y_e < 0.35$ outflows while moderate to higher entropy $30 < s/k < 100$, larger electron fraction $0.35 < Y_e < 0.48$ outflows show partial r-processing for these nuclei.

The distribution of influential neutron capture rates in the $A = 80$ region depends critically on the r-process path which is set by these conditions. Low entropy simulations tend to pile up more material at the $N = 50$ closed shell and so exhibit important neutron capture rates at lower atomic mass compared to high entropy simulations, see Figures 3 and 5 respectively.

In agreement with previous studies of neutron capture rates in a main r process, we show that neutron capture rates of individual nuclei in a weak r process are significant only once (n, γ)-(γ, n) equilibrium breaks down and the neutron-to-seed ratio drops below unity. We also find both the early time freezeout photodissociation mechanism and the late freezeout neutron capture mechanism are active in this region.

A complete description of the $A = 80$ abundances we find in nature is fraught with compilations. These light elements may owe their origins to a range of nucleosynthesis processes including the weak r-process models studied here. The resolution of isotopic abundances in low metallicity halo stars will help settle this issue however these observations alone will not be enough. The reduction of large nuclear physics uncertainties, such as those found in neutron capture rates, is critical for accurately predicting final abundance patterns.[41] Direct (n, γ) measurements are not possible with the very short-lived nuclear species pointed out in this work. Indirect techniques such as (d, p) or Coulomb dissociation measurements can be employed, though further development is required to connect this type of experimental data to the thermal cross sections used in r-process calculations. Thus improvements in theoretical models of neutron capture are needed along with the advances in experiment to reduce these key nuclear physics uncertainties.

[1] M. E. Burbidge, G. R. Burbidge, W. A. Fowler, and F. Hoyle, Rev. Mod. Phys. **29**, 547 (1957).
[2] A. G. W. Cameron, Chalk River Rep. **CRL-41** (1957).
[3] G. Wallerstein *et al.*, Rev. Mod. Phys. **69**, 995 (1997).
[4] F. Käppeler, R. Gallino, S. Bisterzo, and W. Aoki, Rev. Mod. Phys. **83**, 157 (2011).
[5] M. Arnould and S. Goriely, Phys. Rep. **384**, 1 (2003).
[6] F.-K. Thielemann *et al.*, J. Phys.: Conference Series **202**, 012006 (2010).
[7] M. Arnould, S. Goriely, and K. Takahashi, Phys. Rep. **450**, 97 (2007).
[8] G. J. Wasserburg, M. Busso, and R. Gallino, Astrophys. J. **446**, L109 (1996).
[9] J. J. Cowan, I. Roederer, C. Sneden, and J. E. Lawler, RR Lyrae Stars, Metal-Poor Stars, and the Galaxy, Carnegie Observatories Astrophysics Series, Vol. 5 (2011).
[10] A. Arcones and F. Montes, Astrophys. J. **731**, 5 (2011).
[11] J. S. Thomas *et al.*, Phys. Rev. C **71**, 021302 (2005).
[12] J. S. Thomas *et al.*, Phys. Rev. C **76**, 044302 (2007).
[13] S. D. Pain *et al.*, PoS (NICX) 142 (2008).
[14] K. L. Jones *et al.*, Phys. Rev. C **84**, 034601 (2011).
[15] R. L. Kozub *et al.*, Phys. Rev. Lett. **109**, 172501 (2012).
[16] S. Ahn *et al.*, "Application of accelerators in research and industry: Twenty-Second International Conference," AIP Conference Proceedings **1525**, 541 (2013).
[17] B. Manning *et al.*, *Proceedings of the Fifth International Conference on Fission and Properties of Neutron-Rich Nuclei* (World Scientific, 2013), pp. 570–573.
[18] J. R. Beene *et al.*, J. Phys. G **38**, 024002 (2011).

[19] J. Beun, J. Blackmon, W. R. Hix, G. C. McLaughlin, M. Smith, and R. Surman, J. Phys. G **36**, 025201 (2009).

[20] R. Surman, J. Beun, G. C. McLaughlin, and W. R. Hix, Phys. Rev. C **79**, 045809 (2009).

[21] M. Mumpower, G. C. McLaughlin, and R. Surman, Phys. Rev. C **86**, 035803 (2012).

[22] S. Brett, I. Bentley, N. Paul, R. Surman, and A. Aprahamian, Eur. Phys. J. A **48**, 184 (2012).

[23] R. Surman, M. Mumpower, J. Cass, and A. Aprahamian, *Proceedings of the Fifth International Conference on Fission and Properties of Neutron-Rich Nuclei* (World Scientific, 2013), pp. 538–545.

[24] T. Rauscher, N. Dauphas, I. Dillmann, C. Fröhlich, Z. Fülöp, and G. Gyürky, Rep. Prog. Phys. **76**, 066201 (2013).

[25] M. Pignatari, R. Gallino, M. Heil, M. Wiescher, F. Käppeler, F. Herwig, and S. Bisterzo, Astrophys. J. **710**, 1557 (2010).

[26] S. Goriely, Phys. Lett. B **436**, 10 (1998).

[27] R. Surman and J. Engel, Phys. Rev. C **64**, 035801 (2001).

[28] T. Rauscher, Nucl. Phys. A **758**, 655 (2005).

[29] K. Farouqi, K.-L. Kratz, B. Pfeiffer, T. Rauscher, and F.-K. Thielemann, American Institute of Physics Conference Series **819**, 419 (2006).

[30] A. Arcones and G. Martínez-Pinedo, Phys. Rev. C **83**, 045809 (2011).

[31] Y.-Z. Qian and S. E. Woosley, Astrophys. J **471**, 331 (1996).

[32] R. Surman, G. C. McLaughlin, and W. R. Hix, Astrophys. J **643**, 1057 (2006).

[33] M. Mumpower, G. C. McLaughlin, and R. Surman, Phys. Rev. C **85**, 045801 (2012).

[34] R. D. Hoffman, S. E. Woosley, G. M. Fuller, and B. S. Meyer, Astrophys. J **460**, 478 (1996).

[35] C. Sneden, J. J. Cowan, and R. Gallino, Ann. Rev. Astron. Astrophys. **46**, 241 (2008).

[36] R. Surman, G. C. McLaughlin, M. Ruffert, H.-Th. Janka, and W. R. Hix, Astrophys. J. **679**, L117 (2008).

[37] R. H. Cyburt *et al.*, Astrophys. J Suppl. **189**, 240 (2010).

[38] T. Rauscher and F.-K. Thielemann, At. Data Nucl. Data Tables **75**, 1 (2000).

[39] W. R. Hix and F.-K. Thielemann, J. Comput. Appl. Math. **109**, 321 (1999).

[40] S. Wanajo and H.-Th. Janka, Astrophys. J **746**, 180 (2012).

[41] M. Mumpower, G. C. McLaughlin, and R. Surman, Astrophys. J **752**, 117 (2012).